Spectral Characteristics of Instrumental and Climate Model Surface Temperatures

Hege-Beate Fredriksen and Kristoffer Rypdal

Department of Mathematics and Statistics, University of Tromsø, Tromsø, Norway

ABSTRACT

The spatiotemporal temperature variability for several gridded instrumental and general circulation climate model data is characterized, contrasting power spectra of local and global temperatures, land and sea temperatures, and temperatures of different regions. There is generally a high degree of agreement between the spectral characteristics of instrumental and climate model data. All but the equatorial spectra exhibit a power-law shape and are hence more consistent with the spectra expected from long-memory processes than from short-memory processes. The power-law exponent β of the spectra is a measure of memory, or persistence, of the temperatures and is observed to be about twice as large for global temperature than for local temperatures. However, there are large variations, in particular between land and sea surface temperatures. This is shown by estimates of the spectra for different regions and global maps of β. It is also demonstrated that global spectra are related to local spectra via teleconnections between local temperatures.

1. Introduction

This paper aims to characterize spatiotemporal variability of surface temperatures by studying their spectral properties. We will analyze several gridded instrumental data and long control runs from a selection of climate models, and we will systematically study the differences between local and global temperatures and between land and sea surface temperatures.

Recent analyses show that long-range memory (LRM) stochastic processes are good models for Earth surface temperatures. This is confirmed in many climate model and instrumental data for both globally and hemispherically averaged temperatures (Rypdal and Rypdal 2014; Rypdal et al. 2013; Rybski et al. 2006; Østvand et al. 2014; Lennartz and Bunde 2009) and many local temperatures (Blender and Fraedrich 2003; Fraedrich and Blender 2003; Huybers and Curry 2006; Rybski et al. 2008; Franzke 2010; Koscielny-Bunde et al. 1998). The physical origin of the long memory

appears to be a delayed energy exchange between different parts of the climate system, in particular between the surface and the deeper oceans (Fraedrich and Blender 2003; Fraedrich et al. 2004; Rypdal 2012; Rypdal and Rypdal 2014). However, a systematic study of the differences in the memory properties on local, global, and intermediate spatial scales has yet to be made.

Stationary long-range memory processes are characterized by autocovariance functions of the power-law form: $\gamma(\tau) \propto \tau^{\beta-1}$, where τ is the time lag and $0 < \beta < 1$ is a scaling exponent characterizing the persistence, or memory, of the process. It is related to the commonly used Hurst exponent H by $\beta = 2H - 1$. Since $\beta > 0$, the function decays so slowly to zero as $\tau \to \infty$ that the integral over it will be infinite, and the temperature will depend strongly on past temperatures also for the long time scales, hence, the notion of long-range memory. A long-range memory model also implies the power-law form of the power spectral density $S(f) \propto f^{-\beta}$. The power spectral density diverges as $f \to 0$, but the spectral power for frequencies lower than f is $\int_0^f S(f') \, df' \sim f^{1-\beta} \to 0$ as $f \to 0$. The dominance of the low frequencies in the spectral density is a manifestation of the long-range memory, and the power-law shape signifies the scale invariance or scaling of the stochastic process. One important break of scaling is the seasonal variation recorded in local and regional

data. These variations are commonly subtracted from the temperature records before spectral analysis is performed. In contrast, we have the short-range memory (SRM) models, such as the autoregressive processes of first order [AR(1)], which exhibit weaker dependence on the long time scales. An AR(1) process has a finite autocorrelation time τ_c and exhibits a Lorentzian spectrum that is flat for $f \ll \tau_c^{-1}$ and approaches f^{-2} for $f \gg \tau_c^{-1}$. Lack of memory at longer time scales implies that the system will relax to equilibrium at time scales longer the τ_c if it is not subjected to further forcing. However, Rypdal and Rypdal (2014) demonstrate that the presence of long memory may prevent relaxation to an equilibrium state even at centennial time scales if the climate system is subject to persisting anthropogenic forcing.

The spectral properties in this paper will be estimated by computing the periodogram of global temperatures, and of local and regionally averaged temperatures from different regions. From these spectra we will estimate and plot the spectral exponent β in a global map. Maps showing the spatial distribution of locally estimated β have been made for some datasets (Vyushin et al. 2012; Blender and Fraedrich 2003; Fraedrich and Blender 2003; Huybers and Curry 2006; Franke et al. 2013). Some of these papers, including Monetti et al. (2003), also point out that there is a clear difference between the spectral exponents observed for continental interiors and those observed for sea surface temperatures. For land areas β could be as low as zero, while for sea surface temperatures it can approach unity. Furthermore, Huybers and Curry (2006) suggest that β decreases with increasing latitude and that it is tightly linked to the strength of the seasonal variations.

In the existing literature β for global temperature is estimated to be in the range 0.8–0.9, which is higher than for most local temperatures. A fractional energy balance model (FEBM) was proposed by Rypdal et al. (2015) that yields LRM behavior of both local and global temperatures and β for global temperature twice that of local temperatures. This simple model treats a uniform spherical Earth surface with an LRM temporal response and horizontal transport modeled by a linear diffusion term. This model does not take into account large regional differences. In the present paper, we explore further how well the observational data, and data from atmosphere–ocean general circulation models (AOGCMs), are described by the FEBM.

Section 2 gives an overview of the datasets used in this paper; section 3 describes how we estimate the spectrum and relates the spectrum for global temperature to the spectra for local temperatures. The results

TABLE 1. The instrumental and reanalysis datasets. In the rows where several datasets are specified, the second name is that of the SST dataset and the third is that of the land temperature dataset. For the other datasets, land and sea are separated using a land mask. (CRUTEM4 = Climatic Research Unit Temperature, version 4.)

Dataset	No. of grid boxes	Time (yr)
20CRv2	180×91	1871–2012
HadCRUT4, HadSST3, and CRUTEM4	72×36	1850–2014
BEST	15 984	1850–2014
GISTEMP (1200 km), ERSST, and GISTEMP (250 km)	180×90 (89)	1880 (1854)–2014
NOAA MLOST	72×36	1880–2014

are presented in section 4, followed by discussions and conclusions in section 5.

2. The datasets

a. Instrumental data

The three most widely used gridded temperature datasets—HadCRUT4 (Morice et al. 2012), GISTEMP (Hansen et al. 2010), and NOAA Merged Land–Ocean Surface Temperature Analysis (MLOST) (Smith et al. 2008)—are all analyzed in this paper. In addition, we have analyzed the relatively new dataset Berkeley Earth Surface Temperature (BEST) (Rohde et al. 2013a,b). All the datasets were downloaded in November 2014, and some details about the datasets can be found in Table 1. In the following we will briefly describe the construction of these datasets, since it will be of importance for the final statistical properties.

All the datasets have included some land temperature data from the Global Historical Climatology Network (GHCN) (Peterson and Vose 1997), but various other sources of land temperatures are also used. In total, around 5000–7000 stations are included, except for BEST, which includes almost 37 000 stations. All the datasets incorporate sea surface temperature (SST) observations from the Comprehensive Ocean–Atmosphere Dataset (COADS) (Slutz et al. 1985; Woodruff et al. 2011). Hence, the sources of observational data employed in the construction of the different datasets probably have some overlap, but there are many differences in how the data are processed in the construction of a global gridded temperature dataset. Both GISTEMP and NOAA MLOST are based on the same gridded SST dataset, the Extended Reconstructed Sea Surface Temperature (ERSST) (Smith et al. 2008). HadCRUT4 incorporates the sea surface data the Hadley Centre

SST, version 3 (HadSST3) (Kennedy et al. 2011a,b), and a modified version of HadSST3 is also used by BEST.

In the construction of all datasets, there were some quality control and bias corrections. BEST applies pure statistical techniques when processing the land temperature observations. Rather than adjusting the records, they are split into several subrecords at the points where a bias is suspected, and each is treated separately (the scalpel approach; Rohde et al. 2013b). The methods employed for interpolating the records in the construction of a global gridded field also differ among the datasets. BEST uses kriging, which is also known as Gaussian process regression (see Rohde et al. 2013b and references therein); HadCRUT4 employs no interpolation; and GISS Surface Temperature Analysis (GISTEMP) interpolates temperatures in a radius of 1200 km, with weights decreasing linearly with distance from the point. NOAA MLOST employs a more complex routine, involving splitting up the data into low- and high-frequency components, and tuning data to a climate model. The low-frequency components are interpolated in $25° \times 25°$ boxes.

The methods employed to analyze the data in this paper require contiguous time series, but the observational data contain many gaps. So, we have to either disregard the gappy time series or try to fill these gaps. We have chosen to do a combination of these two, because we also want to keep the information from the time series that are almost complete. To fill the gaps, we have copied a segment of the same length as the gap from another part of the time series and spliced it in the gap. The segment was chosen to minimize the discontinuities at the ends of the gap. Since many of the missing data are at the start of a time series, we have chosen to disregard all data before the first segment of at least six contiguous measurements. We retain only for analysis time records that, after this processing, are contiguous over a time interval longer than 1200 months. The method is tested on synthetic fractional Gaussian noises, removing data at random and splicing data back in according to the method described. No large biases are observed for the temporal statistics. An important issue in this paper is to study scaling properties of the time series after different degrees of spatial averaging. To compute such averages, some data gaps can be tolerated in the individual local data records. Hence, we perform those averages on the unprocessed records in order to avoid destruction of spatial correlation through the splicing procedure. Gaps are filled only if there are some remaining after averaging.

b. Reanalysis data

Reanalysis data are included in our studies to explore how their statistics compare with the statistics for the gappy observational data. The Twentieth Century Reanalysis, version 2 (20CRv2) (Compo et al. 2011), is chosen since it is the longest available reanalysis data series, ranging from January 1871 to December 2012. Other widely used reanalyses extend no longer back in time than 1948 and are considered too short for our purpose of studying long-term dependencies. As for all other datasets in the present study, we have chosen the monthly average surface temperatures.

The 20CRv2 data were computed using the ensemble Kalman filter data assimilation system. First, an atmospheric climate model was run to generate a first-guess background field, with sea surface temperatures and sea ice data from the Hadley Centre as lower boundary conditions. Then observations of synoptic surface pressure were used to adjust the first-guess field in an iterative manner to fit the observations better. This process resulted in a complete $2° \times 2°$ spatial field of temperatures, which is more convenient to work with than pure observational data, although the results may be less reliable.

c. Climate model data

A selection of control runs from phase 5 of the Coupled Model Intercomparison Project (CMIP5) with lengths of 500 years or more is analyzed (Taylor et al. 2012). In addition, we have analyzed a 1000-yr control run from the ECHO-G model (Zorita et al. 2003), a coupled model using the ECHAM4 atmosphere and HOPE ocean models. Fraedrich and Blender (2003) and Fraedrich et al. (2004) have previously documented LRM properties of this model, so we think it is interesting to investigate how the latest climate models compare with this one. Some details about the models are found in Table 2.

A major source of uncertainty of the long-term variability observed in these control runs is model drift. As discussed by Sen Gupta et al. (2013), drift refers to

TABLE 2. The climate model control runs. (Expansions of acronyms are available at http://www.ametsoc.org/PubsAcronymList.)

Model	No. of grid boxes	Length (yr)
ECHO-G (Zorita et al. 2003)	96×48	1000
CanESM2 (Chylek et al. 2011)	128×64	996
CCSM4 (Gent et al. 2011)	288×192	501
CNRM-CM5 (Voldoire et al. 2013)	256×128	850
GFDL CM3 (Donner et al. 2011)	144×90	500
IPSL-CM5A-LR (Dufresne et al. 2013)	90×90	1000
MIROC-ESM (Watanabe et al. 2011)	128×64	630
MPI-ESM-LR (Raddatz et al. 2007)	192×96	1000
MPI-ESM-P (Raddatz et al. 2007)	192×96	1156
MRI-CGCM3 (Yukimoto et al. 2011)	320×160	500
NorESM1-M (Bentsen et al. 2013)	144×96	501

spurious long-term changes not related to forcing or internal long-term variability. There can be several causes for this, like numerical errors, or that the system is not in equilibrium for diverse reasons. Spinups of models are done to reduce such errors, but it may take thousands of years for the deep oceans to fully equilibrate, so these errors are hard to get rid of. It is not possible to categorically distinguish between what is drift and what is natural variability. Perhaps it is not even possible to accurately estimate the long-term variability without influences of previous disturbances of the climate system, since the models cannot be initialized from a perfect equilibrium state. Sen Gupta et al. (2013) recommends using as long of portions of the time series as possible when estimating a drift to reduce the chance of mistakenly taking natural variability to be a drift, so we chose to reduce possible effects of drifts by subtracting linear trends from the full records.

3. Methods

a. The periodogram spectral estimator

The power spectral density (PSD) of a discrete-time, stationary, stochastic process $\{T(t)\}$, for $t = 1, 2, \ldots, \infty$ can be defined by

$$S(f) = \lim_{n \to \infty} \frac{\mathbb{E}[|\tilde{T}_n(f)|^2]}{n}, \tag{1}$$

where n is a positive integer and $\tilde{T}_n$ is the discrete Fourier transform of $T(t)$ on the interval $t \in [1, n]$. The symbol $\mathbb{E}$ denotes the expectation value, which in physics literature is often conceived as an ensemble average, that is, an average over an (infinite) ensemble of independent realizations of the stochastic process. Usually we do not have many realizations of the process but have to estimate the PSD from one realization. The periodogram is an estimator for the PSD for evenly sampled time series of length n and is defined by

$$\hat{S}_n(f) = \frac{|\tilde{T}_n(f)|^2}{n}. \tag{2}$$

For the finite-length time series ($n < \infty$), the frequency f is discrete and takes the values $f_m = m/n$, where $m \in \{-n/2, -n/2 + 1, \ldots, n/2 - 1, n/2\}$. The periodogram has a poor signal-to-noise ratio, making the power in individual peaks uncertain. However, this is not a problem for us, since we are only interested in studying the shape of the smoothed spectrum. In our analyses we will also reduce the noise by log binning, that is, an averaging over frequencies within equally wide bins in a log–log plot. By presenting the periodogram in a log–log plot, the scaling exponent β can be estimated by a linear fit to the power spectrum: $\log S(f) = -\beta \log f + c$. The log binning ensures that each time scale is weighted equally.

b. Local, regional, and global spectra

The gridded temperature fields consist of local temperature time series $\{T_i(t)\}$, for $i = 1, \ldots, N$ and $t = 1, \ldots, n$, representing the temperature associated with grid box i. Here n is the length of the time series and N is the total number of grid boxes on the globe. If we spatially average these temperature time series over a region with area A (a continent, an ocean, or the entire globe) and weight each temperature by the area A_i of each grid cell, we obtain a time series averaged over the area $A = \sum_{i=1}^{N_A} A_i$. This averaged temperature series is

$$T_A(t) = \frac{1}{A} \sum_{i=1}^{N_A} A_i T_i(t), \tag{3}$$

which has the power spectral density

$$S_A(f) = \lim_{n \to \infty} \frac{\mathbb{E}[|\tilde{T}_A(f)|^2]}{n}, \tag{4}$$

where $\tilde{T}_A(f)$ denotes the Fourier transform of $T_A(t)$.

c. The influence of spatial dependence on regional and global spectra

The $S_A(f)$ is the weighted sum of all the spectra and cross spectra of the regional temperatures:

$$
\begin{aligned}
S_A(f) &= \lim_{n \to \infty} \frac{\mathbb{E}[\tilde{T}_A(f)\tilde{T}_A(f)^*]}{n} = \lim_{n \to \infty} \frac{\mathbb{E}\left\{\left[\sum_{i=1}^{N_A} A_i \tilde{T}_i(f)\right]\left[\sum_{j=1}^{N_A} A_j \tilde{T}_j(f)\right]^*\right\}}{nA^2} \\
&= \lim_{n \to \infty} \frac{\mathbb{E}\left[\sum_{i=1}^{N_A}\sum_{j=1}^{N_A} A_i A_j \tilde{T}_i(f)\tilde{T}_j(f)^*\right]}{nA^2} = \frac{1}{A^2}\sum_{i=1}^{N_A}\sum_{j=1}^{N_A} A_i A_j S_{ij}(f),
\end{aligned}
\tag{5}
$$

where

$$S_{ij}(f) = \lim_{n \to \infty} \frac{\mathbb{E}[\tilde{T}_i(f)\tilde{T}_j(f)^*]}{n} \qquad (6)$$

is the cross-power spectrum between the time series in cells i and j. An estimator for the cross spectrum is the cross periodogram,

$$\hat{S}_{ij}(f) = \frac{\tilde{T}_i(f)\tilde{T}_j(f)^*}{n}. \qquad (7)$$

Equation (5) expresses the PSD of the spatially averaged temperature record as a weighted sum over all the cross spectra, that is, the sum over all elements in the matrix $(A_i A_j / A^2) S_{ij}(f)$. If there were no spatial correlations between Fourier transforms, then the off-diagonal elements would be zero, and $S_A(f)$ would simply be the trace of this matrix. In general the off-diagonal elements are nonzero, the matrix is Hermitian ($S_{ij} = S_{ji}^*$), and the matrix

$$C_{ij}(f) = \frac{A_i A_j}{A^2} \begin{cases} [S_{ij}(f) + S_{ij}(f)^*], & \text{for} \quad i \neq j \\ S_{ii}(f), & \text{for} \quad i = j \end{cases} \qquad (8)$$

is real and symmetric. For $i \neq j$, each entry of $C_{ij}(f)$ represents the contribution to $S_A(f)$ from the correlations between the spatial locations i and j at the frequency f. The equation $S_{ii}(f) = S_i(f)$ is the PSD of the local temperature $T_i(t)$, and $C_{ii}(f) = (A_i/A)^2 S_i(f)$ is the contribution from the PSD in grid cell i to $S_A(f)$. If we again consider the case of no spatial correlations, then $S_A(f)$ reduces to

$$S_A^{\text{self}}(f) = \sum_{i=1}^{N_A} C_{ii}(f) = \left(\frac{1}{A}\right)^2 \sum_{i=1}^{N_A} A_i^2 S_i(f), \qquad (9)$$

which is just a weighted average of the local spectra. If all of the grid cells had the same area ($A_i = A/N_A$), then this reduces further to the simple average $S_A^{\text{self}}(f) = (1/N_A)\overline{S}_A(f)$, where $\overline{S}_A(f) = (1/N_A)\sum_{i=1}^{N_A} S_i(f)$ is the average local spectrum in the region A. This shows that in the absence of spatial correlations the power in the temperature averaged over an area is inversely proportional to the magnitude of this area. In the presence of spatial correlations, the contributions from the off-diagonal terms cause a smaller reduction in the power with increasing area.

In principle $C_{ij}(f)$ can of course be negative and hence give a negative contribution to $S_A(f)$. However, from Eq. (6) we observe that we get a nonzero cross-spectral power after performing the ensemble average indicated by the symbol $\mathbb{E}$ if the phases $\varphi_i(f)$ and $\varphi_j(f)$ of $\tilde{T}_i(f)$ and $\tilde{T}_j(f)$, respectively, are correlated.

Assuming for simplicity of the argument that the moduli $|\tilde{T}_i(f)|$ and $|\tilde{T}_j(f)|$ are approximately constant over the ensemble, we can write

$$C_{ij}(f) \approx \lim_{n \to \infty} \frac{A_i A_j}{A^2} \frac{|\tilde{T}_i(f)||\tilde{T}_j(f)|}{n} 2\mathbb{E}[\cos\Delta\varphi_{ij}(f)], \qquad (10)$$

where $\Delta\varphi_{ij}(f) = \varphi_i(f) - \varphi_j(f)$. If the phases are perfectly correlated, then we have $\Delta\varphi_{ij}(f) = 0$ and hence $\mathbb{E}[\cos\Delta\varphi_{ij}(f)] = 1$. If they are perfectly uncorrelated, then $\cos\Delta\varphi_{ij}(f)$ will have random values in the interval $[-1, 1]$, and $\mathbb{E}[\cos\Delta\varphi_{ij}(f)] = 0$. If they are correlated, but not perfectly, $|\Delta\varphi_{ij}(f)|$ is typically less than $\pi/2$ in an ensemble member and hence $0 < \mathbb{E}[\cos\Delta\varphi_{ij}(f)] < 1$. This implies that typically $C_{ij} \gtrsim 0$ and that it contributes positively to the spectral density of the spatially averaged signal $S_A(f)$. Ensemble averaging is usually not what we do when performing estimation, but the argument can easily be transferred to averaging over nearby frequencies. Let us rewrite Eq. (5) in the form

$$S_A(f) = S_A^{\text{self}}(f) + \sum_{i=1}^{N_A} S_i^{\text{corr}}(f), \qquad (11)$$

where

$$S_i^{\text{corr}}(f) = \frac{1}{2} \sum_{j=1}^{N_A} C_{ij}(f)(1 - \delta_{ij}) \qquad (12)$$

contributes to $S_A(f)$ from the correlations between the grid cell i and all of the other grid cells within region A. If A represents the entire globe, then a plot of $S_i^{\text{corr}}(f)$ as a function of i will reveal information about how strongly the variability on the frequency f at each location is teleconnected to the variability on this frequency over the rest of the globe.

The term $\sum_{i=1}^{N_A} S_i^{\text{corr}}(f)$ in Eq. (11) modifies the shape of the local PSDs given by $S_A^{\text{self}}(f)$. The spatial correlations are stronger on longer time scales, so $S_i^{\text{corr}}(f)$ has more power on the low frequencies. In the FEBM described in Rypdal et al. (2015), this increased power on low frequencies effectively retains the power-law shape but enhances the spectral exponent β.

4. Results

a. Globally averaged local PSDs and PSDs of global average

In Figs. 1 and 2 we show local and global temperature spectra for many instrumental and climate model data. This is done separately for land and sea surface
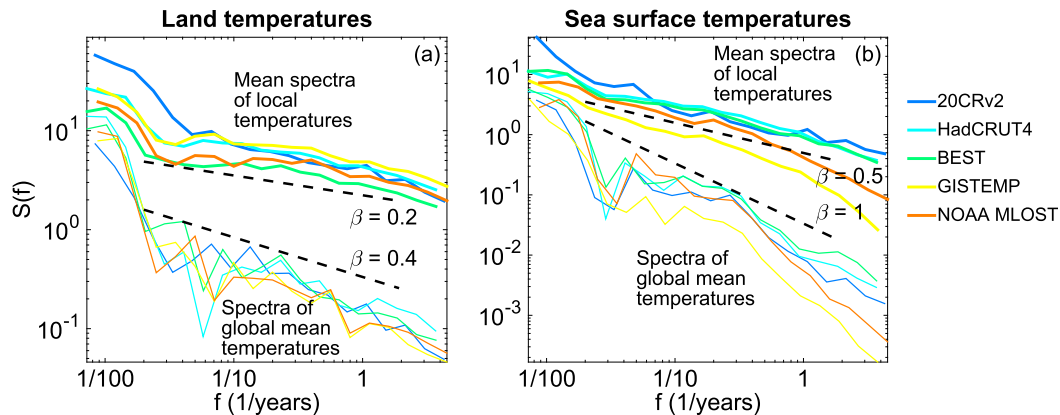
FIG. 1. The mean local and global spectra for (a) land temperatures and (b) SSTs. All temperatures are detrended prior to the analysis to reduce the influence from anthropogenic warming.

temperatures, since their spectra differ substantially. On time scales up to about 20 yr, the scaling characteristics in observational or reanalysis spectra and the model spectra are remarkably consistent. The general tendency is that the spectral slopes increase and that the power density decreases as one moves from local to global scales. For land, the local spectral index β is approximately 0.2 and the global-average index is approximately 0.4. For sea, the corresponding values are 0.5 and 1.0. These tendencies are consistent with the theoretical discussion in section 3c and are in quantitative agreement with the results derived from the FEBM of Rypdal et al. (2015).

The average local spectra for instrumental data exhibit lower high-frequency variability than the spectra for control runs but comparable low-frequency variability. This can be explained by the fact that most of the grid cells in the climate models are smaller than the grid cells for the instrumental data. As we will discuss further

below, there is also large variations among spectra for local instrumental temperatures.

When considering globally averaged temperatures, the power for observational or reanalysis data and model data is similar for the highest frequencies, despite that model data are averaged over a larger area than observational data. Some of the observed sea surface temperatures show even lower high-frequency power than the model data. In Figs. 3j,k and 4j,k, we observe that the average over the equatorial region contains less high-frequency variability than the global average. This implies that missing observational values at high latitudes give the equatorial temperatures more weight in a global average, hence reducing high-frequency variability for observed global temperature.

On longer time scales, the global observational and reanalysis data contain more power than the global model data; the former contains more power on the century time scale than derived from the scaling
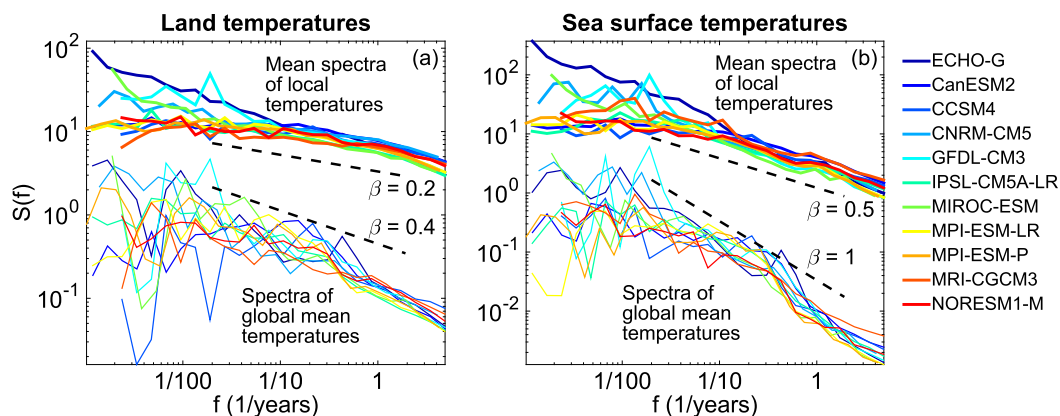

FIG. 2. The mean local and global spectra for (a) land temperatures and (b) SSTs. All temperatures are linearly detrended to reduce possible drifts in the climate models.
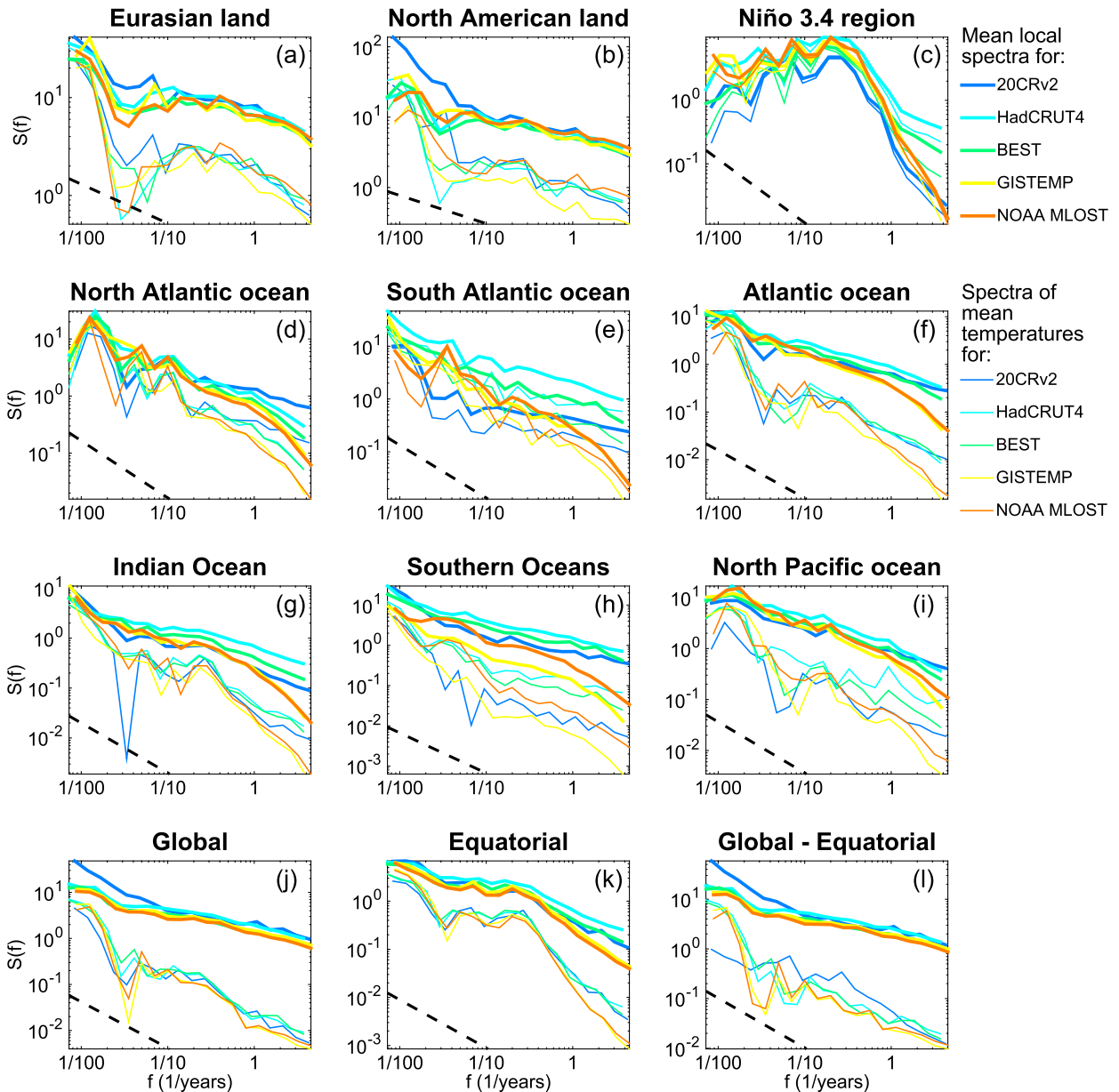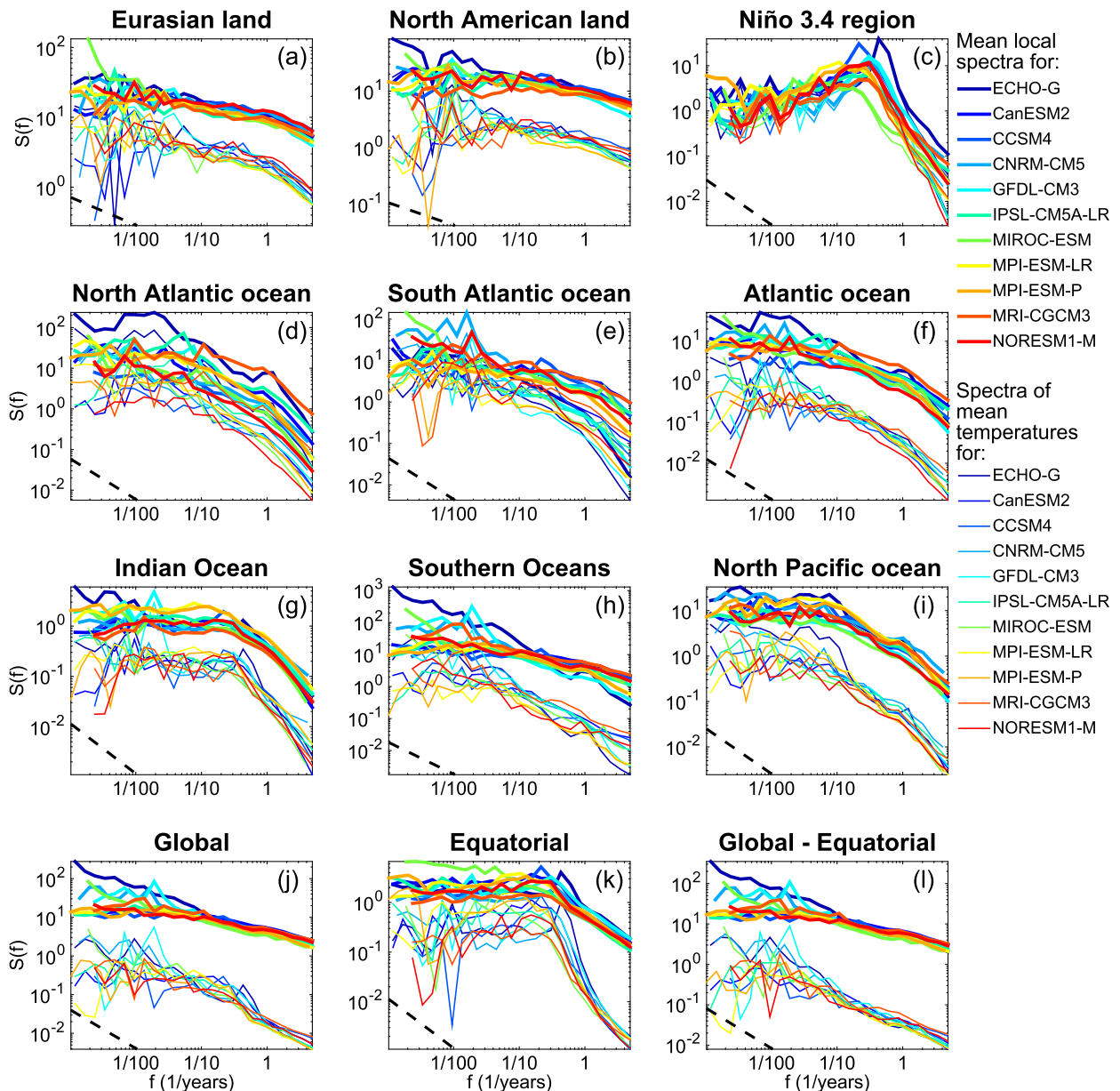
FIG. 3. The mean local spectra in several regions specified in Table 3. The thick lines are the mean spectra of the local temperatures, while the thin lines are the spectra of the mean temperature in the region. All temperatures are linearly detrended to reduce the anthropogenic influence. The black dashed lines are reference lines with (a),(b) $\beta = 0.4$ for the land-only temperatures and (c)–(l) $\beta = 1$. Note that the range of $S(f)$ is different for each panel.

slope, whereas the latter contains less. One cannot conclude from this, however, that the models do not reproduce correctly the variability on these time scales. There are two reasons for this; the first is that the model simulations are control runs and do not reflect variability caused by external forcing. The detrended observational records, on the other hand, are influenced by the component of the forcing that is not eliminated by the linear detrending. The second

reason is that the model data are averaged over a larger area than the instrumental data, and the power may hence be generally lower just because of the averaging.

That said, it is quite evident that the larger power on multidecadal scales in the observational data is due to the oscillation with a period around 70 yr that is observed in the instrumental records. This oscillation is well described by the Atlantic multidecadal oscillation

FIG. 4. The mean local spectra in several regions specified in Table 3. The thick lines are the mean spectra of the local temperatures, while the thin lines are the spectra of the mean temperature in the region. All temperatures are linearly detrended to reduce possible drifts in the climate models. The black dashed lines are reference lines with (a),(b) $\beta = 0.4$ for the land temperatures and (c)–(l) $\beta = 1$. Note that the range of $S(f)$ is different for each panel.

(AMO), which is probably linked to the Atlantic Ocean circulation (McCarthy et al. 2015). AMO is possibly present in the control runs as well, since there are no large differences between models and observations in the mean local spectra. But if it is present, there must be regions included in the mean temperature for the models that have a similar oscillation out of phase with the regions included in the average for observations. In that way, the variability on a global scale can be partially

averaged out and produce the lower power observed for model data on the long time scales.

b. Regionally averaged local PSDs and PSDs of regional average

Some regions have been selected for study, as specified in Table 3. For each of these regions, the mean spectrum of the local temperatures and the spectrum of the mean temperature are estimated. The resulting

TABLE 3. Specifications of regions used in Figs. 3 and 4.

Region	Lat	Lon
Global	90°S–90°N	All longitudes
Equatorial	20°S–20°N	All longitudes
Global without equatorial	20°–90°S and 20°–90°N	All longitudes
Eurasian land	40°–90°N	Eastern Hemisphere
North American land	40°–90°N	180°–60°W
North Atlantic Ocean	40°–60°N	50°–10°W
South Atlantic Ocean	40°–60°S	50°W–0°
Atlantic Ocean	60°S–60°N	60°W–0°
Niño-3.4 region	5°S–5°N	170°–120°W
Indian Ocean	40°S–20°N	40°–120°E
North Pacific Ocean	20°–60°N	120°E–120°W
Southern oceans	40°–90°S	All longitudes

spectra are plotted for observational data in Fig. 3 and for model data in Fig. 4. The overall absolute values of the slopes (β) of the thin lines displaying the log–log spectra for average temperatures are in general higher, and the total power lower, than the corresponding features shown by the thick lines for the averaged local spectra. The increased β after spatial averaging are in agreement with the predictions from the FEBM of Rypdal et al. (2015), and the reduced power follows from Eq. (9) and the subsequent discussion.

For most of the regions the spectra are close to power laws. The land regions have higher power and lower β than all of the ocean regions, as we have already observed for global mean land and sea in Figs. 1 and 2. The largest deviations from a power-law spectrum are found in the eastern equatorial Pacific Ocean, which exhibits increased power at time scales of a few years due to the dynamics of El Niño–Southern Oscillation (ENSO). At longer time scales these spectra appear flat and are hence closer to what we can expect from short-range memory processes, for example, as in Ault et al. (2013). Since ENSO also has an influence on other areas near the equator, the same tendencies are observed for spectra for all equatorial temperatures.

The general agreement between spectra for observations or reanalyses and control runs in all regions is remarkable, although the model spectra are more variable. The most apparent discrepancy seems to be that the spectral peak due to the 70-yr oscillation (related to the AMO) seems to disappear in the spatially averaged model temperatures, while it prevails in the corresponding averaged instrumental temperatures. This indicates that this oscillation is more spatially coherent in the instrumental observations than in the model control runs.

In many regions, the spectra observed for the various control runs are quite similar, and the variability among the simulations do not seem to depend systematically on the size of the grid boxes. However, in the Atlantic, and in particular in the North Atlantic, the variability is larger than elsewhere. There is also some variability in the power on centennial time scales in the southern oceans.

From the theory in section 3c and the results discussed in section 4a, we should expect temperatures from the datasets with the large grid boxes to have a slightly higher β and less power than temperatures given in small grid boxes, if the temperatures were representative average temperatures over the areas of the grid boxes. Both HadCRUT4 and NOAA MLOST are given on a 5° × 5° grid and hence should have similar statistics. So should the Twentieth Century Reanalysis and GISTEMP, both of which are given on a 2° × 2° grid. BEST is difficult to compare, since it has larger grid boxes than other datasets near the poles and it has smaller grid boxes near the equator. By studying the thin lines in Fig. 3, we observe that there is no systematic difference between the local spectra for datasets given on a 5° × 5° grid and the datasets given on a 2° × 2° grid. The spectra for the Eurasian and North American land temperatures are all very similar, with some exceptions for the reanalysis data, but for sea surface temperatures there are large variations. The power in HadCRUT4 temperatures is quite high, while the spectra for NOAA MLOST seem to be more comparable to those derived from GISTEMP. The latter can probably be explained by the fact that both GISTEMP and NOAA MLOST are based on the same data for sea surface temperatures. The higher values of the spectra of HadCRUT4 may be attributed to the lack of spatial interpolation, making this a more local dataset.

The variations of spatial coverage could explain some differences between the spectra for the observational and reanalysis datasets, in particular for averaged temperatures. Datasets with a higher degree of spatial interpolation allow for averaging over larger areas. The good coverage of land temperatures compared to sea surface temperatures makes the degree of interpolation less important for land than for sea, and it is likely important for understanding why sea surface temperatures vary more between the datasets than land temperatures.

The differences between spectra of observational and model data could also be partially explained by the larger data coverage in the models than in the observations. We observe for instance particularly high power
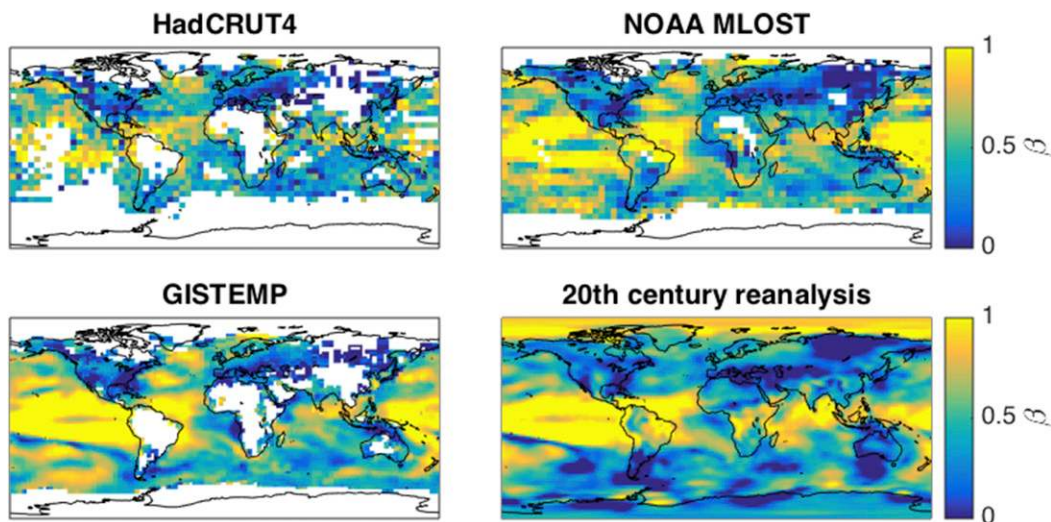
FIG. 5. Spectral exponent β estimated from the periodogram of linearly detrended instrumental and reanalysis datasets on time scales between 1 and 10 yr.

for the reanalysis data on the low frequencies for North American temperatures. This can be explained by a steep warming near the Arctic in the latter half of the time series that will not be fully removed by a linear detrending of the entire time series. In this region we do not have sufficient observations to include statistics from the instrumental datasets.

c. Long-range memory in temperature data

Since most of the spectra are close to straight lines in log–log plots, we can estimate the persistence of the temperatures by fitting straight lines to the log–log periodograms. The slopes of the lines will be $-\beta$, and in Fig. 5 we estimate β for three gridded observational data and the Twentieth Century Reanalysis data. Only frequencies corresponding to time scales between 1 and 10 yr are used here, since the statistics at long time scales are poor for these short records. Figures 6 and 7 show β estimated for the control runs on time scales between 1 and 10 yr and between 10 and 100 yr, respectively. As we noticed in Figs. 3 and 4, there are some regions where the spectra deviate from a power law, so the values estimated for β should be interpreted with care. In particular, the fits on time scales between 1 and 10 yr in the eastern equatorial Pacific will be poor, because the lines will be fitted through the ENSO peak. The estimated slope in most of this region will be very high as a result of the steep increase of the spectrum toward this peak. In some cases the slope could also be estimated to be negative.

These plots confirm our previous results of a lower persistence over land than over sea, at least for the

Northern Hemisphere. In the Southern Hemisphere, we find many values of β for land that are comparable to those found for sea. Except for Antarctica, the majority of landmasses in the Southern Hemisphere are at low latitudes, where the atmospheric circulation is largely influenced by the Hadley cell and the Walker cell, causing more persistent wind patterns. Because of this and the weak weather noise forcing, North et al. (2011) argue that the tropical length scales are much longer than elsewhere. Moreover, landmasses in the Southern Hemisphere are more fragmented and hence more likely to be influenced by sea surface temperatures.

On the longest time scales, we could have effects of drift in the control runs, so we have done a linear detrending prior to the analysis in order to reduce possible drift effects. We have also performed the analysis without the detrending (not shown), and the results are almost the same in that case. The southern oceans in the MIROC-ESM are an exception, where trends result in higher values of β. The values of β estimated on time scales between 10 and 100 yr are generally lower than those estimated between 1 and 10 yr. The strongest persistence on the long time scales is found in the southern oceans and in the North Atlantic. Some of the strong centennial variability in the southern oceans is possibly linked to ocean–sea ice interactions, causing abrupt surface temperature changes in the Weddell Sea (Martin et al. 2013), where the time interval between each abrupt change is on the order of centuries. There are also some regions with negative values of β and others with $\beta \approx 0.5$. On these multidecadal time scales,
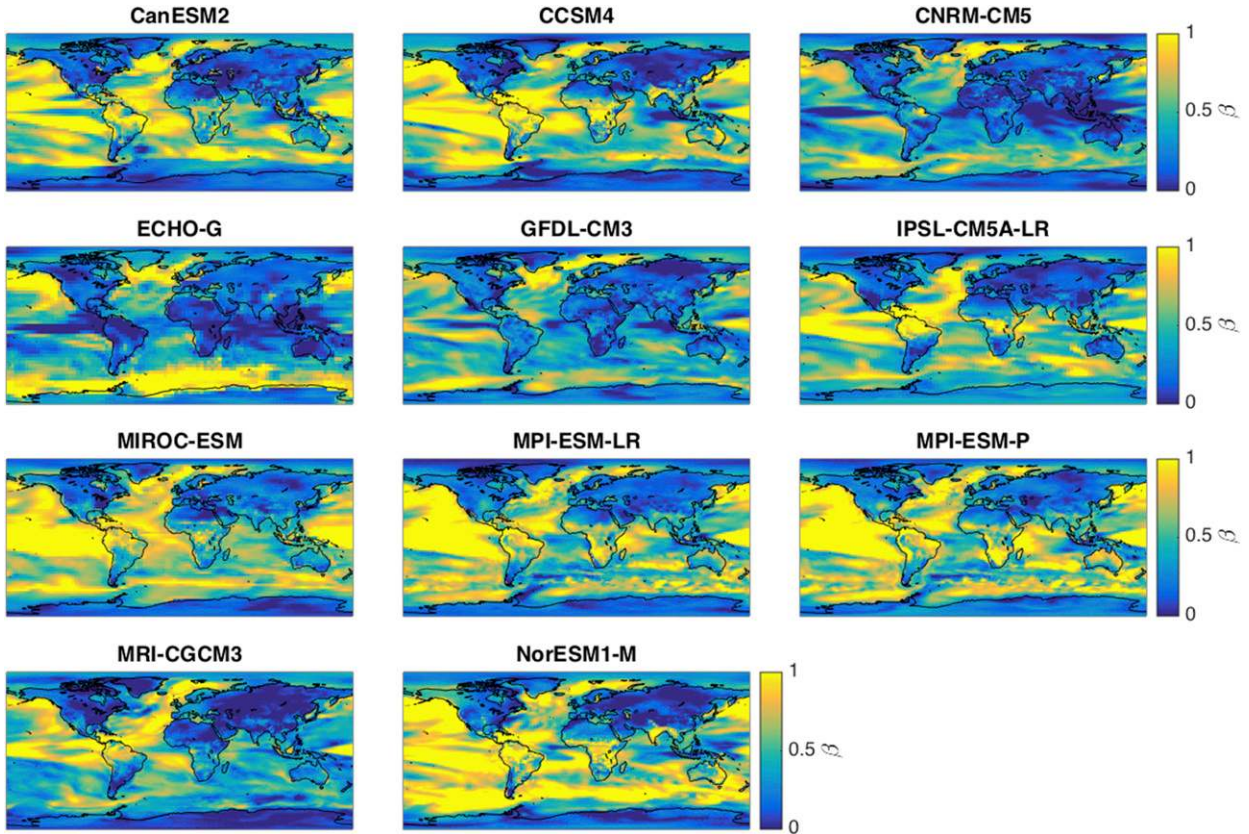
FIG. 6. Spectral exponent β estimated from the periodogram of temperatures from climate model control runs on time scales between 1 and 10 yr.

there is no systematic difference between land and sea surface temperatures.

In Fig. 4 the ECHO-G model is seen to exhibit stronger long-term variability than the CMIP5 models, particularly in the North Atlantic and the southern oceans. Its strong variability is also observed in Fig. 7 as high values of β. Our results hence confirm previous findings of LRM in this model (Fraedrich and Blender 2003; Fraedrich et al. 2004). Other models also show the presence of LRM on global scales and in most regional temperatures, but it seems to be weaker for the CMIP5 models analyzed here than for ECHO-G. The differences can probably be attributed to further developments of the climate models since the ECHO-G run was completed, including the removal of the additional heat and freshwater flux used to correct for drifts in ECHO-G.

d. Regions with strong teleconnections in NorESM1-M

In this subsection we consider data from the control run of NorESM1-M and compute the following estimator for each grid cell i:

$$\hat{\mathcal{S}}_i(f_1, f_2) = \sum_{j=1}^{N} \frac{A_i A_j}{nA^2(f_2 - f_1)} \int_{f_1}^{f_2} \tilde{T}_i(f)\tilde{T}_j(f)^* df, \qquad (13)$$

where n is the length of the time series. The sum $\sum_i \hat{\mathcal{S}}_i(f_1, f_2)$ is the mean power density of the global mean temperature in the frequency band $f_1 < f < f_2$. Hence, $\hat{\mathcal{S}}_i(f_1, f_2)$ is the contribution from each grid cell i to the mean spectrum of global temperature over the specified frequency range and depends on the strength of its teleconnection to other parts of the globe, as measured by the sum of the cross spectra. The diagonal elements of the matrix in Eq. (13)—that is, when $j = i$—represent the area-weighted auto-power spectral density in the frequency band in the grid cell i, and a global map is plotted for different ranges of time scales $1/f_2 < \tau < 1/f_1$ in Fig. 8. The full sum over the diagonal and cross-diagonal elements (the cross powers) is between two and three orders of magnitude larger and is plotted in Fig. 9. This demonstrates that cross power (teleconnections) on the time scale in question contributes much more to the power in the global mean temperature than the auto-power in the respective grid cells. However, the maps in
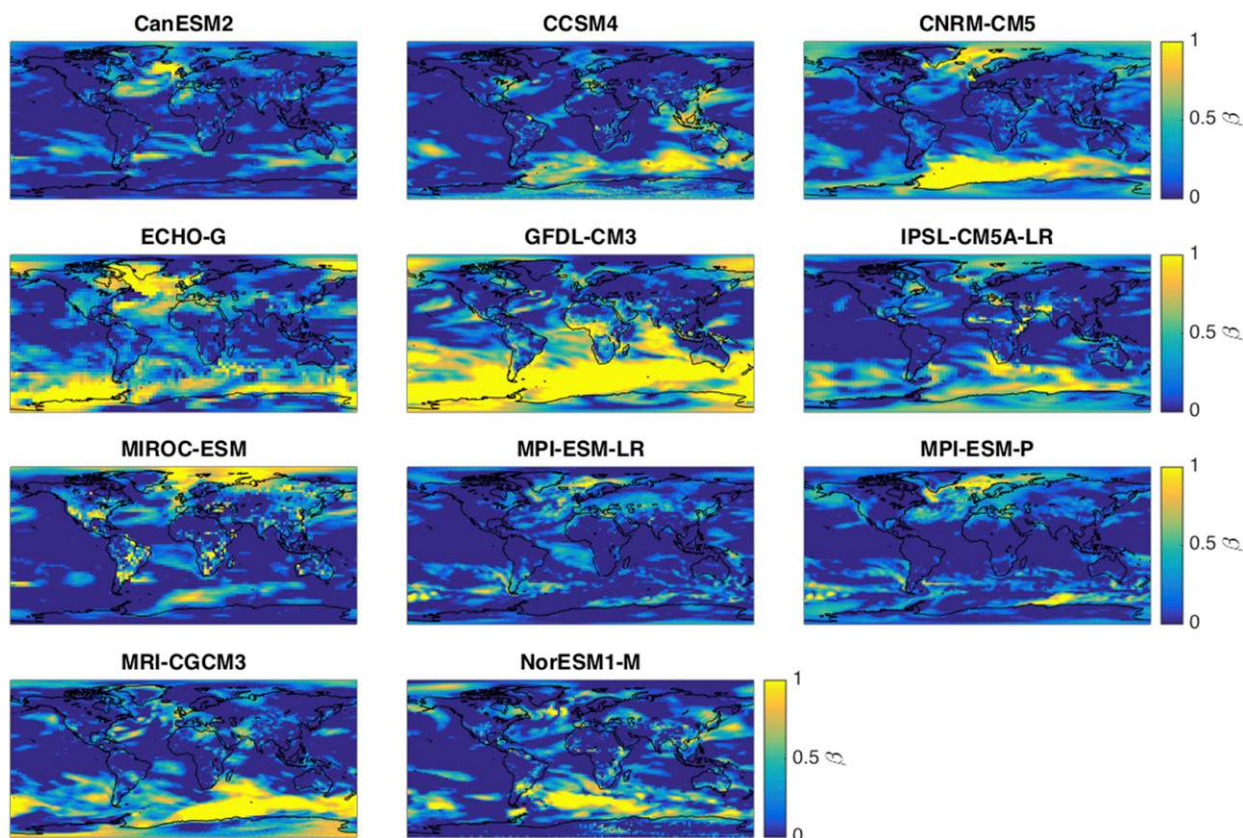
FIG. 7. Spectral exponent β estimated from the periodogram of linearly detrended temperatures from climate model control runs on time scales between 10 and 100 yr.

Figs. 8 and 9 have quite similar structure, indicating that regions with high spectral auto-power in a given frequency band also contribute more to the power of global mean temperature in this band.

For the time scales $0.5 < \tau < 1.5$ yr, continental interiors, in particular Eurasia and North America, contribute strongly to the power in global mean temperature, consistent with the observation in Figs. 3 and 4 of land temperatures having more power than other regions on these time scales. On time scales $2 < \tau < 4$ yr, the eastern equatorial Pacific plays of course a large role. The dynamics of ENSO is known to have an impact on the climate more or less everywhere, and our results suggest that it could have especially strong couplings to Australia and to the northwest region of the United States, although we need to explore the entire cross-power matrix to draw a firm conclusion on this point. As we increase the time scale, we have fewer frequencies to analyze in the estimated spectrum, so we have averaged over longer time scales to reduce the uncertainty. For $20 < \tau < 40$ yr, there is high power in the North Pacific, similar to what is observed for the Pacific decadal

oscillation (Mantua et al. 1997) and some smaller structures in other parts of the world. At the very longest time scales, regions contribute more evenly, although there are some areas in the southern oceans that still have higher power.

Note that although most points have positive values, there are some regions with negative values as well. Equation (10) suggests that such negative contributions can arise from teleconnections more or less in antiphase. Another interesting feature of this figure is the small influence from Antarctica on all time scales, suggesting that no essential interior variability is left out if we compute global temperature without values from Antarctica. This may not be true for forced variability. The methodology employed in this section could be useful for those who want to construct global temperatures and need to determine the relative weights from each region in the global average.

5. Discussion and conclusions

There have been some discussions in the literature as to whether surface temperatures are best described by a
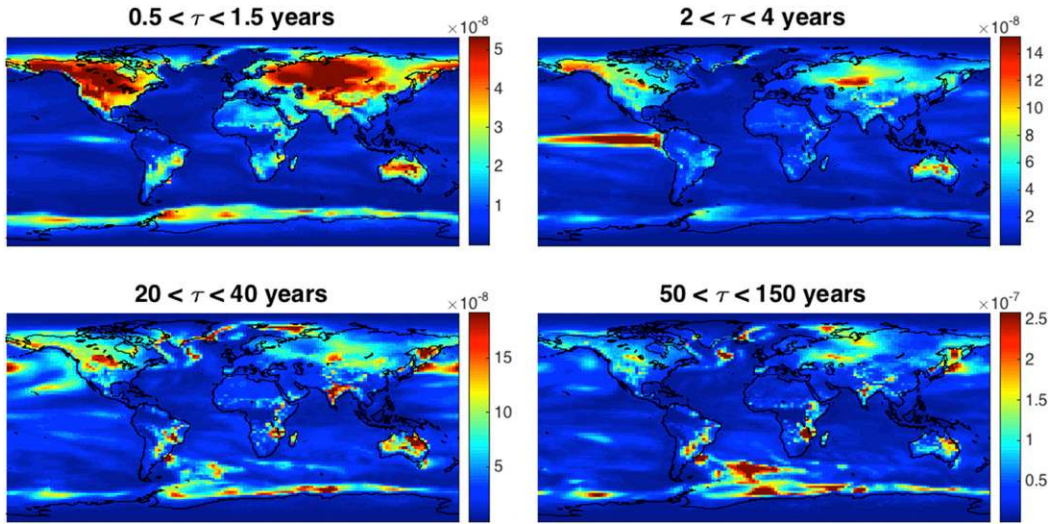
FIG. 8. The average area-weighted power of NorESM1-M surface temperatures in each grid box on the given time scales.

short-range or a long-range memory process (Vyushin et al. 2012). We have shown here that log–log spectra for equatorial temperatures have a steep slope for high frequencies but are flat for lower frequencies, reasonably consistent with a Lorentzian spectrum. Nonequatorial temperature spectra seem to be better described by a long-range persistent process, since the spectra continue to increase with decreasing frequency, even at frequencies corresponding to centennial time scales. Some spectra exhibit a weaker slope at lower frequencies and are perhaps best described by something in between these two classes of

stochastic models, consistent with the conclusions of Vyushin et al. (2012). There are, however, indications that climate models produce internal low-frequency variability that is too low at regional scales (Laepple and Huybers 2014), particularly at low latitudes. When considering an average over many local temperatures, or an average over many local spectra, a reasonable straight-line fit to a log–log spectrum is possible, both for models and observations.

Land temperatures are in general less persistent than sea surface temperatures. Interior land temperatures over large continents like Eurasia and North America
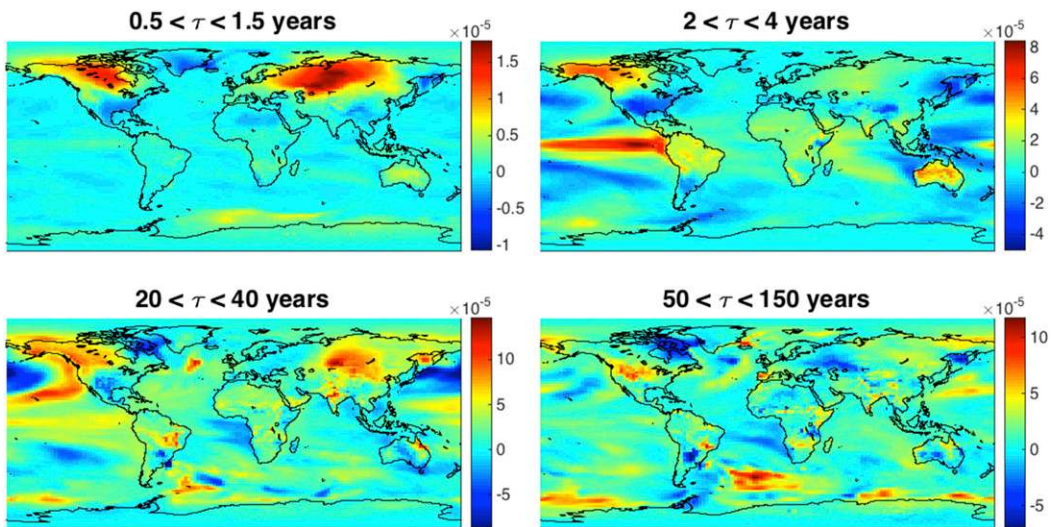

FIG. 9. The weighted sum of the spectrum and all the cross spectra at each grid point *i* for NorESM1-M, as given by Eq. (13).

are well approximated by a white noise, while the persistence is somewhat higher at the coast, in agreement with previous studies (Blender and Fraedrich 2003; Fraedrich and Blender 2003). Land temperatures close to the equator seem to be more persistent as a result of the strong influence of ENSO.

Our results suggest that most of the latitudinal dependence of β observed by Huybers and Curry (2006) can be explained by the strong influence of ENSO closer to the equator. Because of ENSO, characterizing the spectrum in equatorial regions by one single slope does not make much sense. Sea surface temperatures exhibit higher β than land temperatures because of the high thermal inertia of the ocean. Land temperatures experience a stronger seasonal cycle than sea surface temperatures because of the small heat capacity of the land surface. This means that if we exempt regions strongly influenced by ENSO, then the correlation observed by Huybers and Curry (2006) between β and the strength of the annual cycle can be explained by the different thermal inertia of land and sea, without invoking their suggested nonlinear cascade driven by the latitude-dependent seasonal forcing.

When averaging temperatures over a larger area, we observe that the power spectral density decreases, and it decreases more for the high frequencies than for the low frequencies. This is because high-frequency variability is generally more localized in space and will be reduced by spatial averaging. A consequence is that the persistence of the temperature increases with the degree of spatial averaging. As for most of our other results, the equatorial region is exceptional, in this case because it shows a very small decrease of ENSO frequencies compared to higher frequencies.

The local spectral power of the gridded data analyzed in this paper does not depend systematically on the size of the grid boxes, perhaps partly because local and regional variability is similar up to some spatial scale that is larger than the size of the grid boxes. For the observational data, however, we find that temperatures from datasets with large grid boxes may exhibit larger variability than temperatures from small grid boxes, which is contrary to our expectations. We suspect this may be due to the different degree of spatial interpolation used when constructing the datasets. Interpolation in space could have similar effects as averaging over space, hence causing temperatures to effectively represent an average over a larger or smaller area than the area of its grid box. Further analysis needs to be done to determine whether datasets represent variability correctly according to their grid size. If HadSST3 happens to have more local characteristics than an ideal $5° × 5°$ dataset should have, then it could partially explain why Laepple and Huybers

(2014) observe a discrepancy between regional climate model variability and observations from HadSST3. The discrepancy they observe is particularly clear in the North Atlantic. This is also where we observe the largest spread among models, implying that at least some of the models could produce too weak regional variability.

The analysis made in this paper demonstrates a remarkable general agreement between the power spectral characteristics of local, regional, and global temperatures derived from instrumental, reanalysis, and global circulation model data. With the exception of the equatorial region, local and regional power spectra are well described by a power law on time scales from months to centuries, which suggests describing the temperature time series as realizations of long-memory stochastic processes. The spectral exponent β, which measures the degree of long-range memory, is much greater over oceans than over land, and β increases with the degree of spatial averaging, yielding a β for global temperature that is generally twice that for local temperatures. This is due to increased spatial coherence with increasing time scale, and it lends additional observational support to the fractional energy balance model of Rypdal et al. (2015). In this model this increased spatial coherence appears as a result of long-range memory in the temporal response, which can be interpreted as a result of a delayed energy exchange between the surface and other components of the climate system with long response times. Since the model is linear and horizontal energy transport is represented by a simple diffusion term, a nonlinear (turbulent) cascade is not invoked in explaining the spatiotemporal spectral characteristics and the power-law nature of the spectra.

REFERENCES

Ault, T. R., C. Deser, M. Newman, and J. Emile-Geay, 2013: Characterizing decadal to centennial variability in the equatorial Pacific during the last millennium. *Geophys. Res. Lett.*, **40**, 3450–3456, doi:10.1002/grl.50647.

Bentsen, M., and Coauthors, 2013: The Norwegian Earth System Model, NorESM1-M—Part 1: Description and basic evaluation of the physical climate. *Geosci. Model Dev.*, **6**, 687–720, doi:10.5194/gmd-6-687-2013.

Blender, R., and K. Fraedrich, 2003: Long time memory in global warming simulations. *Geophys. Res. Lett.*, **30**, 1769, doi:10.1029/2003GL017666.

Chylek, P., J. Li, M. K. Dubey, M. Wang, and G. Lesins, 2011: Observed and model simulated 20th century Arctic temperature variability: Canadian Earth System Model CanESM2. *Atmos. Chem. Phys. Discuss.*, **11**, 22 893–22 907, doi:10.5194/acpd-11-22893-2011.

Compo, G. P., and Coauthors, 2011: The Twentieth Century Reanalysis Project. *Quart. J. Roy. Meteor. Soc.*, **137**, 1–28, doi:10.1002/qj.776.

Donner, L. J., and Coauthors, 2011: The dynamical core, physical parameterizations, and basic simulation characteristics of the atmospheric component AM3 of the GFDL global coupled model CM3. *J. Climate*, **24**, 3484–3519, doi:10.1175/2011JCLI3955.1.

Dufresne, J.-L., and Coauthors, 2013: Climate change projections using the IPSL-CM5 Earth System Model: From CMIP3 to CMIP5. *Climate Dyn.*, **40**, 2123–2165, doi:10.1007/s00382-012-1636-1.

Fraedrich, K., and R. Blender, 2003: Scaling of atmosphere and ocean temperature correlations in observations and climate models. *Phys. Rev. Lett.*, **90**, 108501, doi:10.1103/PhysRevLett.90.108501.

——, U. Luksch, and R. Blender, 2004: 1/f model for long-time memory of the ocean surface temperature. *Phys. Rev.*, **70E**, 037301, doi:10.1103/PhysRevE.70.037301.

Franke, J., D. Frank, C. C. Raible, J. Esper, and S. Bronnimann, 2013: Spectral biases in tree-ring climate proxies. *Nat. Climate Change*, **3**, 360–364, doi:10.1038/nclimate1816.

Franzke, C., 2010: Long-range dependence and climate noise characteristics of Antarctic temperature data. *J. Climate*, **23**, 6074–6081, doi:10.1175/2010JCLI3654.1.

Gent, P. R., and Coauthors, 2011: The Community Climate System Model version 4. *J. Climate*, **24**, 4973–4991, doi:10.1175/2011JCLI4083.1.

Hansen, J., R. Ruedy, M. Sato, and K. Lo, 2010: Global surface temperature change. *Rev. Geophys.*, **48**, RG4004, doi:10.1029/2010RG000345.

Huybers, P., and W. Curry, 2006: Links between annual, Milankovitch and continuum temperature variability. *Nature*, **441**, 329–332, doi:10.1038/nature04745.

Kennedy, J. J., N. A. Rayner, R. O. Smith, D. E. Parker, and M. Saunby, 2011a: Reassessing biases and other uncertainties in sea surface temperature observations measured in situ since 1850: 1. Measurement and sampling uncertainties. *J. Geophys. Res.*, **116**, D14103, doi:10.1029/2010JD015218.

——, ——, ——, ——, and ——, 2011b: Reassessing biases and other uncertainties in sea surface temperature observations measured in situ since 1850: 2. Biases and homogenization. *J. Geophys. Res.*, **116**, D14104, doi:10.1029/2010JD015220.

Koscielny-Bunde, E., A. Bunde, S. Havlin, H. Roman, Y. Goldreich, and H.-J. Schellnhuber, 1998: Indication of a universal persistence law governing atmospheric variability. *Phys. Rev. Lett.*, **81**, 729–732, doi:10.1103/PhysRevLett.81.729.

Laepple, T., and P. Huybers, 2014: Global and regional variability in marine surface temperatures. *Geophys. Res. Lett.*, **41**, 2528–2534, doi:10.1002/2014GL059345.

Lennartz, S., and A. Bunde, 2009: Trend evaluation in records with long-term memory: Application to global warming. *Geophys. Res. Lett.*, **36**, L16706, doi:10.1029/2009GL039516.

Mantua, N. J., S. R. Hare, Y. Zhang, J. M. Wallace, and R. C. Francis, 1997: A Pacific interdecadal climate oscillation with impacts on salmon production. *Bull. Amer. Meteor. Soc.*, **78**, 1069–1079, doi:10.1175/1520-0477(1997)078<1069:APICOW>2.0.CO;2.

Martin, T., W. Park, and M. Latif, 2013: Multi-centennial variability controlled by Southern Ocean convection in the Kiel Climate Model. *Climate Dyn.*, **40**, 2005–2022, doi:10.1007/s00382-012-1586-7.

McCarthy, G. D., I. D. Haigh, J. J. M. Hirschi, J. P. Grist, and D. A. Smeed, 2015: Ocean impact on decadal Atlantic climate variability revealed by sea-level observations. *Nature*, **521**, 508–510, doi:10.1038/nature14491.

Monetti, R. A., S. Havlin, and A. Bunde, 2003: Long-term persistence in the sea surface temperature fluctuations. *Physica A*, **320**, 581–589, doi:10.1016/S0378-4371(02)01662-X.

Morice, C. P., J. J. Kennedy, N. A. Rayner, and P. D. Jones, 2012: Quantifying uncertainties in global and regional temperature change using an ensemble of observational estimates: The HadCRUT4 data set. *J. Geophys. Res.*, **117**, D08101, doi:10.1029/2011JD017187.

North, G. R., J. Wang, and M. G. Genton, 2011: Correlation models for temperature fields. *J. Climate*, **24**, 5850–5862, doi:10.1175/2011JCLI4199.1.

Østvand, L., T. Nilsen, K. Rypdal, D. Divine, and M. Rypdal, 2014: Long-range memory in internal and forced dynamics of millennium-long climate model simulations. *Earth Syst. Dyn.*, **5**, 295–308, doi:10.5194/esd-5-295-2014.

Peterson, T. C., and R. S. Vose, 1997: An overview of the Global Historical Climatology Network temperature database. *Bull. Amer. Meteor. Soc.*, **78**, 2837–2849, doi:10.1175/1520-0477(1997)078<2837:AOOTGH>2.0.CO;2.

Raddatz, T., and Coauthors, 2007: Will the tropical land biosphere dominate the climate–carbon cycle feedback during the twenty-first century? *Climate Dyn.*, **29**, 565–565, doi:10.1007/s00382-007-0247-8.

Rohde, R., R. Muller, R. Jacobsen, S. Perlmutter, and S. Mosher, 2013a: Berkeley Earth temperature averaging process. *Geoinf. Geostat: An Overview*, **1** (2), doi:10.4172/2327-4581.1000103.

——, and Coauthors, 2013b: A new estimate of the average earth surface land temperature spanning 1753 to 2011. *Geoinf. Geostat: An Overview*, **1** (1), doi:10.4172/2327-4581.1000101.

Rybski, D., A. Bunde, S. Havlin, and H. von Storch, 2006: Long-term persistence in climate and the detection problem. *Geophys. Res. Lett.*, **33**, L06718, doi:10.1029/2005GL025591.

——, ——, and H. von Storch, 2008: Long-term memory in 1000-year simulated temperature records. *J. Geophys. Res.*, **113**, D02106, doi:10.1029/2007JD008568.

Rypdal, K., 2012: Global temperature response to radiative forcing: Solar cycle versus volcanic eruptions. *J. Geophys. Res.*, **117**, D06115, doi:10.1029/2011JD017283.

——, L. Østvand, and M. Rypdal, 2013: Long-range memory in Earth's surface temperature on time scales from months to centuries. *J. Geophys. Res. Atmos.*, **118**, 7046–7062, doi:10.1002/jgrd.50399.

——, M. Rypdal, and H.-B. Fredriksen, 2015: Spatiotemporal long-range persistence in Earth's temperature field: Analysis of stochastic-diffusive energy balance models. *J. Climate*, **28**, 8379–8395, doi:10.1175/JCLI-D-15-0183.1.

Rypdal, M., and K. Rypdal, 2014: Long-memory effects in linear response models of Earth's temperature and implications for future global warming. *J. Climate*, **27**, 5240–5258, doi:10.1175/JCLI-D-13-00296.1.

Sen Gupta, A., N. C. Jourdain, J. N. Brown, and D. Monselesan, 2013: Climate drift in the CMIP5 models. *J. Climate*, **26**, 8597–8615, doi:10.1175/JCLI-D-12-00521.1.

Slutz, R. J., S. J. Lubker, J. D. Hiscox, S. D. Woodruff, R. L. Jenne, D. H. Joseph, P. M. Steurer, and J. D. Elms, 1985: COADS:

Comprehensive Ocean–Atmosphere Data Set, release 1. NOAA Environmental Research Laboratories, Climate Research Program, 262 pp.

Smith, T. M., R. W. Reynolds, T. C. Peterson, and J. Lawrimore, 2008: Improvements to NOAA's historical merged land–ocean surface temperature analysis (1880–2006). *J. Climate*, **21**, 2283–2296, doi:10.1175/2007JCLI2100.1.

Taylor, K. E., R. J. Stouffer, and G. A. Meehl, 2012: An overview of CMIP5 and the experiment design. *Bull. Amer. Meteor. Soc.*, **93**, 485–498, doi:10.1175/BAMS-D-11-00094.1.

Voldoire, A., and Coauthors, 2013: The CNRM-CM5.1 global climate model: Description and basic evaluation. *Climate Dyn.*, **40**, 2091–2121, doi:10.1007/s00382-011-1259-y.

Vyushin, D. I., P. J. Kushner, and F. Zwiers, 2012: Modeling and understanding persistence of climate variability. *J. Geophys. Res.*, **117**, D21106, doi:10.1029/2012JD018240.

Watanabe, S., and Coauthors, 2011: MIROC-ESM 2010: Model description and basic results of CMIP5-20c3m experiments. *Geosci. Model Dev.*, **4**, 845–872, doi:10.5194/gmd-4-845-2011.

Woodruff, S. D., and Coauthors, 2011: ICOADS Release 2.5: Extensions and enhancements to the surface marine meteorological archive. *Int. J. Climatol.*, **31**, 951–967, doi:10.1002/joc.2103.

Yukimoto, S., and Coauthors, 2011: Meteorological Research Institute-Earth System Model version 1 (MRI-ESM1)—Model description. MRI Tech. Rep. 64, 71 pp. [Available online at http://www.mri-jma.go.jp/Publish/Technical/DATA/VOL_64/index_en.html.]

Zorita, E., F. González-Rouco, and S. Legutke, 2003: Testing the Mann et al. (1998) approach to paleoclimate reconstructions in the context of a 1000-yr control simulation with the ECHO-G coupled climate model. *J. Climate*, **16**, 1378–1390, doi:10.1175/1520-0442(2003)16<1378:TTMEAA>2.0.CO;2.